

The Gowdy T^3 Cosmologies revisited

S.D. Hern and J.M. Stewart

Department of Applied Mathematics & Theoretical Physics,
Silver Street, Cambridge CB3 9EW, UK

30 January 1998

Abstract

We have examined, repeated and extended earlier numerical calculations of Berger and Moncrief for the evolution of unpolarized Gowdy T^3 cosmological models. Our results are consistent with theirs and we support their claim that the models exhibit AVTD behaviour, even though spatial derivatives cannot be neglected. The behaviour of the curvature invariants and the formation of structure through evolution both backwards and forwards in time is discussed.

PACS numbers: 04.25.Dm, 04.20.Dw, 98.80.Hw

DAMTP R-97/41

gr-qc/9708038

To appear in Classical and Quantum Gravity

1 Introduction

The Hawking-Penrose theorems [9] imply that every ‘physically reasonable’ cosmological model possesses a singularity; however very little is known about its nature. Early studies due to Belinskii *et al* [1] suggested that the behaviour of the generic singularity resembles that of the spatially homogeneous Bianchi VIII and IX cosmological models, commonly called *mixmaster dynamics*. It is generally felt, however, that matters are not this simple, and attention has focused on the *velocity-term-dominated behaviour* (VTDB) hypothesis due to Eardley *et al* [5]. It is very hard to give a covariant definition but, loosely speaking, the hypothesis claims that near the singularity spatial derivatives play no part in the evolution; locally one has a spatially homogeneous cosmology, but with the parameters varying from point to point. This is the starting point for many large-scale-structure calculations in physical cosmology (see, for example, [15]), but is it correct? If spatial derivatives are ignored, the evolution equations become ordinary differential equations whose behaviour is easier to analyse. Isenberg and Moncrief [10] have introduced an alternative hypothesis of *asymptotically velocity-term dominated* (AVTD) behaviour. A cosmological model is AVTD if its asymptotic behaviour near the singularity is that of the ordinary differential equation system. Clearly VTDB implies AVTD behaviour, but the converse may not be true. In order to test the validity and usefulness of these hypotheses we need to examine the behaviour of inhomogeneous cosmological models, and the simplest examples would appear to be the Gowdy T^3 models [6]. Polarized Gowdy cosmologies exhibit AVTD behaviour [10], and so attention focuses on the less tractable unpolarized case [7], which appears to require numerical treatment.

Berger and Moncrief [3] and Berger [2] (who give much more extensive bibliographies than the brief introduction above) have tackled the unpolarized case numerically. This is a decidedly non-trivial task, and so they introduced novel numerical algorithms, which led them to conclude, tentatively, that the AVTD hypothesis was confirmed. Their grounds for caution are based on the inability of their code to resolve fine-scale spatial structure. As they suggest, this problem requires an algorithm with adaptive mesh refinement (AMR), discussed in section 3.

We have used our AMR code to repeat and extend the earlier calculations. We obtain broadly similar results, but with additional fine structure. We confirm the earlier result that the Gowdy T^3 cosmologies exhibit AVTD behaviour but can find no evidence that the VTDB hypothesis holds universally near the singularity. Our results show that by starting with smooth data and evolving backwards in cosmic time towards the singularity our fields develop complicated spatial structure. If we time-reverse our calculations we appear to be asserting that complicated structure becomes smooth as it evolves into the future, the exact opposite of widespread beliefs in the theory of large-scale structure! We have therefore taken generic smooth data near the singularity and evolved it into the future finding, as expected, that complicated spatial structure appears. The fields that we are discussing are merely metric components with no covariant meaning. We have therefore computed curvature invariants. These become very large near the singularity, but they too have complicated spatial structure, implying that this is not a coordinate effect.

2 The Gowdy T^3 Universe

The line element used by Berger and Moncrief [3] for the Gowdy T^3 cosmology is

$$ds^2 = e^{\lambda/2} e^{\tau/2} (-e^{-2\tau} d\tau^2 + d\theta^2) + e^{-\tau} (e^P d\sigma^2 + 2e^P Q d\sigma d\delta + (e^P Q^2 + e^{-P}) d\delta^2), \quad (2.1)$$

where λ , P and Q are functions of τ and θ only, $-\infty < \tau < \infty$ with $\tau = \infty$ a singularity, and $0 \leq \theta, \sigma, \delta \leq 2\pi$. The functions λ , P and Q are required to be periodic in θ with period 2π . The polarized mode corresponds to $Q = 0$.

The vacuum momentum constraint equation is

$$-\lambda_\theta = 2(P_\tau P_\theta + e^{2P} Q_\tau Q_\theta), \quad (2.2)$$

and the Hamiltonian constraint is

$$-\lambda_\tau = P_\tau^2 + e^{-2\tau} P_\theta^2 + e^{2P} (Q_\tau^2 + e^{-2\tau} Q_\theta^2), \quad (2.3)$$

while the vacuum evolution equations reduce to

$$P_{\tau\tau} = e^{-2\tau} P_{\theta\theta} + e^{2P} (Q_\tau^2 - e^{-2\tau} Q_\theta^2), \quad (2.4a)$$

$$Q_{\tau\tau} = e^{-2\tau} Q_{\theta\theta} - 2(P_\tau Q_\tau - e^{-2\tau} P_\theta Q_\theta). \quad (2.4b)$$

Here $f_\tau = \partial f / \partial \tau$, etc. It should be noted that the evolution equations (2.4) do not involve λ . The energy constraint (2.3) determines λ and the momentum constraint (2.2) is satisfied at all times if it is satisfied initially, provided the other equations hold. As pointed out by Berger and Moncrief [3] the evolution equations are harmonic map equations for a target space with metric

$$dS^2 = dP^2 + e^{2P} dQ^2, \quad (2.5)$$

and so study of these equations is not without interest.

The integration programmes described in the next section require a first order system of equations. We accomplish this by introducing new variables as follows:

$$A = P_\tau, \quad B = Q_\tau, \quad C = P_\theta, \quad D = Q_\theta. \quad (2.6)$$

The system of evolution equations now takes the form

$$A_\tau = e^{-2\tau} C_\theta + e^{2P} (B^2 - e^{-2\tau} D^2), \quad (2.7a)$$

$$B_\tau = e^{-2\tau} D_\theta - 2(AB - e^{-2\tau} CD), \quad (2.7b)$$

$$C_\tau = A_\theta, \quad (2.7c)$$

$$D_\tau = B_\theta, \quad (2.7d)$$

$$P_\tau = A, \quad (2.7e)$$

$$Q_\tau = B, \quad (2.7f)$$

$$\lambda_\tau = -A^2 - e^{-2\tau} C^2 - e^{2P} (B^2 + e^{-2\tau} D^2). \quad (2.7g)$$

The last equation is only needed if λ is to be evolved simultaneously with P and Q , in which case

$$\lambda_\theta = -2(AC + e^{2P}BD) \quad (2.8)$$

from equation (2.2) acts as a constraint.

Initial data at $\tau = 0$ is also required. Berger and Moncrief suggest that the following choice is reasonably generic (with λ chosen to satisfy (2.8)):

$$A = v_0 \cos \theta, \quad B = 0, \quad C = 0, \quad D = -\sin \theta, \quad P = 0, \quad Q = \cos \theta, \quad \lambda = 0, \quad (2.9)$$

and the results reported here use $v_0 = 10$ as used in [3].

3 Numerical Procedures

As we shall see in the next section, the evolution produces structure on fine scales with steep gradients. One numerical strategy is to use a standard algorithm, e.g., Lax-Wendroff, together with a very fine grid structure. This certainly works but it is not the most efficient way to proceed. Berger and Moncrief [3] used a *symplectic integrator*, described in their paper. However their calculation produced fine-scale structure even at sizes comparable with the grid spacing, which they regarded as unreliable. In presenting their results spatial averaging was used to remove the finest-scale structure. An alternative approach is due to van Putten [14], but he reports integration of the equations only for short times and small values of the parameter v_0 in the initial data.

Problems of this type are natural candidates for *adaptive mesh refinement* (AMR), which seeks to add extra grid points when they are needed and to remove them when they become unnecessary. We used an implementation of the Berger and Oliger [4] AMR algorithm which is descended from the one described in Hamadé and Stewart [8]. Numerous changes have been made to that code. Those relevant to this paper are:

- an arbitrary number of grids may exist at each level of refinement;
- it is now possible to switch in arbitrary integrators, giving the code ‘modularity’;
- cubic spline interpolation is preferred to the quadratic interpolation used earlier, thus guaranteeing continuous spatial second derivatives;
- when creating finer grids one can choose to use data from obsolete grids at the same level, rather than relying on interpolation from the parent grid.

For non-specialists, the third change introduces a subtle form of data smoothing, which can be (almost) eliminated by the fourth change.

It is straightforward to write a generalization of the standard Lax-Wendroff two-step algorithm which is second-order accurate for the system (2.7), and this proved to be the fastest choice. (If the typical spatial grid spacing is $\Delta\theta$, then a second-order accurate method produces a local truncation error which is $O((\Delta\theta)^3)$. The mesh refinement is typically $\Delta\theta \rightarrow \Delta\theta/4$, and so a single stage of refinement reduces the local truncation error by nearly two orders of magnitude, as well as enhancing spatial resolution.) In addition (and as part of a long-term programme) we used our interpretation of the second-order accurate wave propagation routine from the CLAWPACK high-resolution package of LeVeque [12]. (CLAWPACK is written in FORTRAN. The administrative part of our code is written in C++, and the numerically intensive functions are written either in C or C++. It proved easier, and more instructive, to adapt the CLAWPACK routines to this environment, rather than to interface the FORTRAN to the existing code.)

For calculations using the Berger-Oliger algorithm the initial coarse grid had a spatial separation $\Delta\theta = 2\pi/2000$. The finest child grid actually used had $\Delta\theta = 2\pi/512\,000$. As a check to ensure that the AMR code was not introducing spurious effects we repeated the calculations with $\Delta\theta = 2\pi/8000$ and no mesh refinement. The Lax-Wendroff and CLAWPACK-like codes were

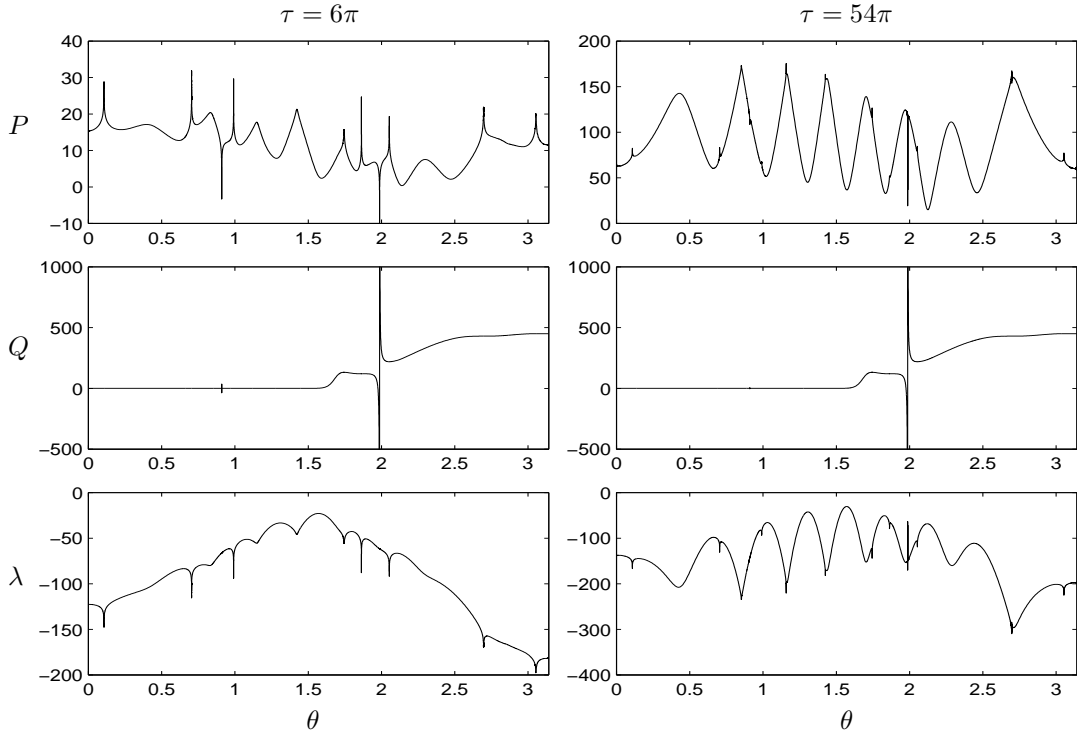


Figure 1: P , Q and λ as functions of θ at two different times. The left column corresponds to $\tau = 6\pi$, the right to $\tau = 54\pi$, and θ ranges from 0 to π . (The problem is invariant under $\theta \rightarrow 2\pi - \theta$, and so only one half of the full θ -range is shown.) The large spikes in Q are truncated by the choice of vertical scale.

developed by the two different authors, continuing our policy to eliminate coding errors. We also checked our codes against the exact pseudo-unpolarized solution

$$P = \log \cosh P_0, \quad Q = \tanh P_0, \quad P_0(\tau, \theta) = J_0(e^{-\tau}) \cos \theta, \quad (3.1)$$

(where J_0 is a Bessel function) given by Berger and Moncrief [3], and confirmed that for both of our integration methods the errors decreased at second order. There were only very small differences between the results from AMR with Lax-Wendroff and those from AMR with CLAWPACK, and what is reported in the next section is common to both.

4 Numerical Results

We are reporting on the integration of equations (2.7) with initial data (2.9) and $v_0 = 10$, the same conditions as used by Berger and Moncrief [3]. (More or less spatial structure develops for larger or smaller, respectively, values of the parameter v_0 . Berger [2] uses $v_0 = 5$ and gets results with a less complicated spatial structure, though with the same basic features.)

The main numerical results of Berger and Moncrief are summarized in figures 4 and 5 of [3]. The left-hand column of our figure 1 shows P , Q and λ as functions of θ at $\tau = 6\pi = 18.85$, the latest time of their figures 4 and 5. The right-hand column of figure 1 shows the variables at a much later time of $\tau = 54\pi = 169.6$. The graphs in figure 1 comprise all available data from the AMR grid hierarchy.

The structure of P becomes complicated soon after the start of the evolution and by time $\tau = 6\pi$ (as figure 1 shows) it includes a number of fine spikes. At first sight these spikes might

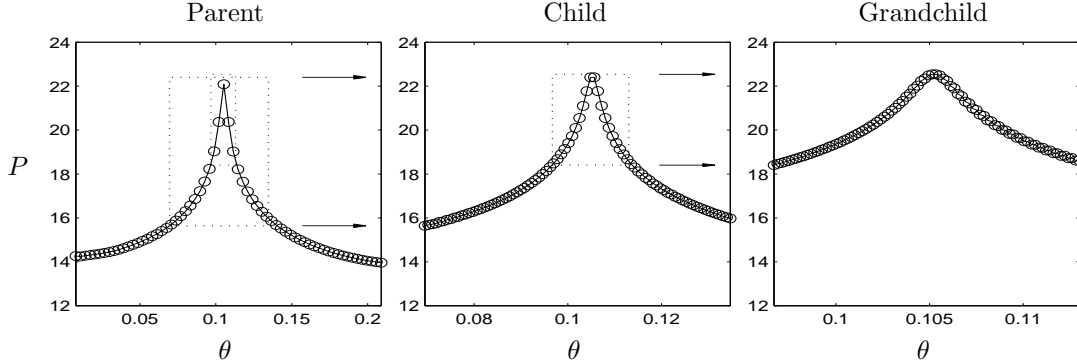


Figure 2: Data from three generations of grids at a spike in P . Each grid has a resolution greater by a factor of four than the grid to its left. Each circle is one grid point, and the dotted boxes show the sizes and data ranges of the subgrids. (The data is taken at time $\tau = 15$.)

seem to be errors in the evolution, and, indeed, when Berger and Moncrief first found spikes in their data, they considered them unreliable and used spatial averaging to remove them from figures 4 and 5 of [3]. However, our AMR code automatically refines the evolution in regions where spikes start to form, increasing the grid resolution so that the spikes appear smooth and the evolution can continue without loss of accuracy. This is demonstrated in figure 2 where data at a spike is shown for a coarse grid and for two refined subgrids. (Notice that on the finer grids the spike reaches a greater height than on the coarse grid. The AMR algorithm uses an average of data from fine grids to update data on coarse grids.)

Spikes form in P in both the positive and negative directions. Examining the development of the positive spikes (the negative spikes are discussed below) it is found that their peaks grow linearly at rates $P_\tau = \text{constant} > 1$, while at the same time they decrease in width. As a spike narrows (and there is no indication that the spikes ever stop growing or narrowing) the AMR code is forced to use finer and finer grids to keep it well resolved until, eventually, it becomes narrower than the smallest grid spacing that the AMR code has been instructed to use, and from that point on it cannot be assumed that the code is accurately evolving the spike. We have to accept that there are probably significant errors in the calculated heights of the spikes in P , but this does not imply that there must be large errors elsewhere in the data: since the characteristic speed of the model is $\exp(-\tau)$, deviations from the exact solution that develop at some time not too soon after the start of the evolution can only propagate very small distances from their points of origin.

At late times $P_{\tau\tau} \equiv A_\tau$ becomes very small, and so A freezes and P grows linearly in time with the spatial profile shown in the right-hand column of figure 1. Except at the points where spikes formed, the spatial profile of P at late times has quite a simple form, much less intricate than early on in its evolution. For reasons discussed above, the numerical simulation is unable to determine the late-time behaviour of the spikes. While small spikes and lumps appear in the graph of P at $\tau = 54\pi$ in figure 1, these are just the residue left by spikes that have narrowed beyond the resolution of the simulation. The spikes themselves, assuming they continued to grow at their initial rates, would go off the scale of the graph.

To suggest reasons for the observed behaviour it is useful to know which are the dominant terms in the governing equations. Here we adopt the definition that a term is *dominant* if its absolute value exceeds ten times the sum of the absolute values of the other terms. Figure 3 illustrates this for the wave equations (2.7a,b) for $A_\tau \equiv P_{\tau\tau}$ and $B_\tau \equiv Q_{\tau\tau}$. The lightly shaded regions in (τ, θ) -space are where the terms $\exp(2P)B^2$ (in (2.7a)) and $-2AB$ (in (2.7b)) dominate the right-hand sides. The darker shaded regions are where the terms $-\exp(2P - 2\tau)D^2$ and $2\exp(-2\tau)CD$ dominate. The narrow black regions are where the terms $\exp(-2\tau)C_\theta$ and $\exp(-2\tau)D_\theta$ dominate. The white regions are where no one term dominates. It is clear from the figure that there is very

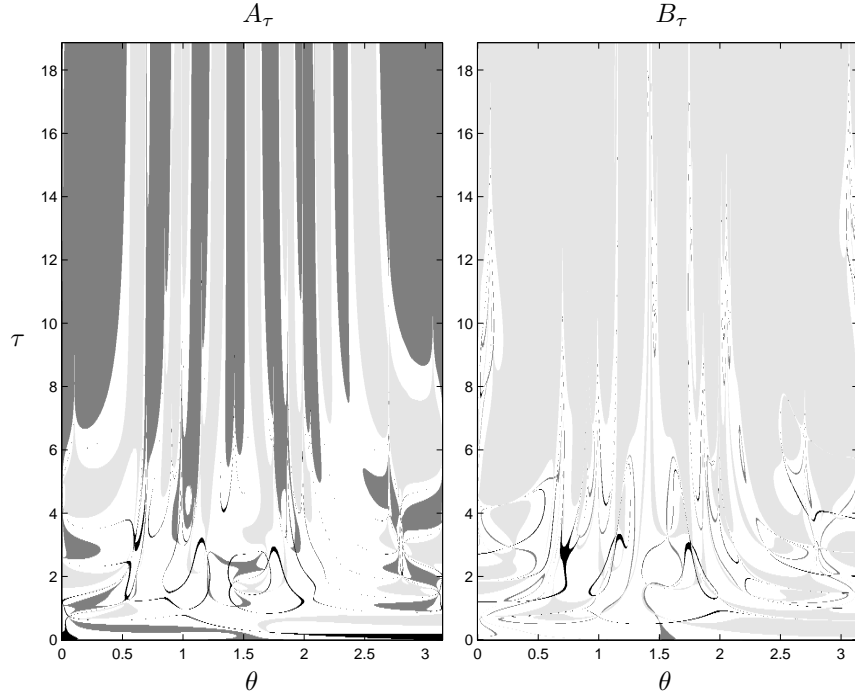


Figure 3: The dominant terms in the A_τ and B_τ equations (2.7a,b) as functions of θ and τ . The black regions are where terms involving C_θ and D_θ dominate, the dark-shaded regions are where terms involving C and D dominate, and the light-shaded regions are where terms involving A and B dominate. In the white regions no single term dominates.

complicated interplay between terms during the early stages of the evolution, and it seems unlikely that the overall behaviour can be traced to simple causes. Berger [2] notes that spikes form at points where $D \equiv Q_\theta = 0$ (though not all such zeros produce spikes) and discusses their formation in terms of bounces off of potentials in the evolution equations. In terms of dominance behaviour, spike formation occurs in dark-grey regions in the left half, and light-grey regions in the right half of figure 3.

Sharp features also form in Q as it evolves. Figure 1 shows that Q at $\tau = 6\pi$ has a negative spike and a positive spike very close together with a steep gradient between the two peaks. A second, similar double-spike feature is also present, but only just visible in figure 1 because of the scale. The positions of the two double spikes in Q coincide with the positions of the two negative spikes in P . A close examination of the data reveals that both the positive and negative peaks of each double spike in Q grow at an exponential rate, while the overall width of the feature becomes smaller, and that the negative spikes in P grow linearly in much the same way that their positive counterparts do. The discussion above regarding the numerical problems caused by the narrowing of spikes applies equally here.

A double-spike feature is also reported in [2] (see especially figure 2 there, but note that it is produced using different initial data), however the explanation given there is not quite convincing. Examination of the dominance data of figure 3, together with similar data for finer grids, reveals that the region around a double spike ($\theta \approx 2$, $\tau > 4$ for the large double spike in figure 1) is light grey for both equations. We may conclude that in this region the terms proportional to $\exp(-2\tau)$ are irrelevant and so

$$A_\tau \approx e^{2P} B^2, \quad B_\tau \approx -2AB. \quad (4.1)$$

A double spike then forms under the conditions of B crossing zero (the exact position of this shows up as a thin white line in both halves of figure 3), while A is negative and P is negative or

small and positive. It follows that $A_\tau \geq 0$ and is small, so that A remains negative and P forms a negative spike. On both sides of the zero, B then grows exponentially, but in opposite directions, and the result is a double spike in Q . Since $A_\tau \geq 0$ the region in which $A < 0$ becomes smaller, and the double spike narrows. (By $\tau = 10$ the light-grey region that supports the growth of the larger double spike is no longer visible in the left half of figure 3.)

Away from the double spikes, $Q_\tau \equiv B$ quickly approaches zero and Q freezes not long after the start of the evolution: the two plots of Q in figure 1 differ only at the double spikes. Because of the narrowing effect, the second double spike is still barely visible on the right half of figure 1 although, extrapolating its initial growth, it should be larger than the vertical scale of the graph.

The evolution of λ shows similar features to the evolution of P (see figure 1). Negative spikes develop in λ at the same points at which positive spikes develop in P and, apart from pointing in a different direction, they show the same behaviour: they grow at a constant rate and they narrow until they no longer can be resolved by the simulation. In contrast, no unusual behaviour seems to develop in λ at the points where double spikes form in Q (although the errors in the data at the double spikes are sufficient to produce erratic behaviour in λ there at late times, as can be seen in figure 1).

Equation (2.7g) shows that λ is a decreasing function of time, and it is clear from figure 1 that λ becomes large and negative as it evolves. At late times, $\lambda_\tau \approx -A^2$ (cf. equation (2.7g)) and A is approximately constant, so λ grows linearly with a fixed spatial profile.

The constraint equation (2.8) in our system relates the spatial derivative of λ to the values of P and Q and their first derivatives. For an exact solution of the evolution equations (2.7) the constraint equation is satisfied at all times if it is satisfied initially, but for a numerical solution this is not necessarily the case. We monitor the degree to which the constraint equation fails to hold by calculating the total percentage error defined by

$$\text{error}(\%) = 100 \int |\lambda_\theta + 2(AC + e^{2P}BD)| d\theta \Big/ \int |\lambda_\theta| d\theta, \quad (4.2)$$

where the integrals are evaluated using the trapezium rule and λ_θ is estimated from λ using second-order finite differencing. Since the errors are known to be disproportionately large at the spikes we do not include these points when measuring the constraint. (A region of width 0.02 is excised at each spike, with about ten percent of the total domain being removed.) At time $\tau = 6\pi$ the error in the constraint is 1.1%. At time $\tau = 54\pi$ the error is 0.97%, smaller because of the overall growth of λ .

Instead of evolving λ with equation (2.7g) we could calculate it at every time step by integrating equation (2.8). This would obviously ensure that the constraint equation is satisfied, and such ‘fully constrained’ approaches are often applied to problems in numerical relativity. However, for this particular problem enforcing the constraint equation in this way would be a very bad idea: the large errors at the spikes would affect the whole of λ rather than being confined to isolated regions.

Our understanding of a spacetime is, in general, advanced more by studying coordinate-independent quantities which have some physical relevance than by studying the components of the metric. For a vacuum spacetime we can use the curvature tensor to construct four independent scalar quantities—the curvature invariants—which we take in the form

$$\begin{aligned} w_I &= \frac{1}{8} C_{\mu\nu\rho\sigma} C^{\mu\nu\rho\sigma}, & w_{III} &= -\frac{1}{16} C_{\mu\nu}{}^{\rho\sigma} C_{\rho\sigma}{}^{\eta\omega} C_{\eta\omega}{}^{\mu\nu}, \\ w_{II} &= \frac{1}{8} C_{\mu\nu\rho\sigma}^* C^{\mu\nu\rho\sigma}, & w_{IV} &= -\frac{1}{16} C_{\mu\nu}^*{}^{\rho\sigma} C_{\rho\sigma}{}^{\eta\omega} C_{\eta\omega}{}^{\mu\nu}, \end{aligned} \quad (4.3)$$

where $C_{\mu\nu\rho\sigma}$ is the Weyl tensor, $\varepsilon_{\mu\nu\rho\sigma}$ is the Levi-Civita tensor and $C_{\mu\nu\rho\sigma}^* \equiv \frac{1}{2} \varepsilon_{\mu\nu\eta\omega} C^{\eta\omega}{}_{\rho\sigma}$.

Figure 4 shows two of the curvature invariants, w_I and w_{II} , evaluated using our data at time $\tau = 6\pi$. The following discussion concentrates on these two quantities since w_{III} and w_{IV} behave qualitatively the same as, respectively, w_I and w_{II} .

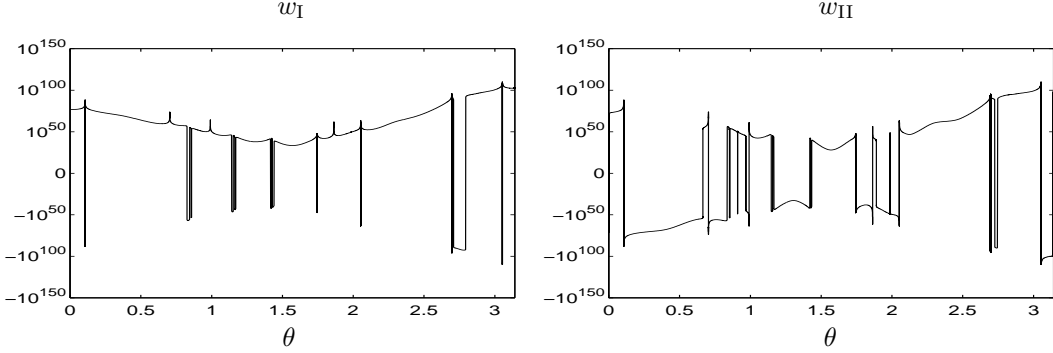


Figure 4: Curvature invariants w_I and w_{II} (see equations (4.3)) at $\tau = 6\pi$ for $0 \leq \theta \leq \pi$. While w_I is invariant under the reflection $\theta \rightarrow 2\pi - \theta$, the sign of w_{II} is reversed. (The data has been scaled using the transformation $w \rightarrow (1/\ln 10) \sinh^{-1}(w/2)$.)

The most striking feature of the curvature invariants is their magnitude: w_I and w_{II} at $\tau = 6\pi$ reach both positive and negative values of size greater than ten to the hundredth power. At the start of the evolution w_I takes values from -50 to $+30\,000$, and w_{II} from -2500 to $+2500$. Their subsequent growth is rapid, and shows no signs of reversing. The main influence on the size of the curvature invariants is the factor $\exp(-\lambda)$ in the expressions for w_I and w_{II} . The effect of λ can be seen by comparing the profiles of w_I in figure 4 and λ at $\tau = 6\pi$ in figure 1. The linear growth (towards minus infinity) of λ at late times corresponds to an exponential growth of the curvature invariants.

As figure 4 shows, the curvature invariants change sign suddenly at various values of θ . These sign changes tend to form into clusters which contract in width as the evolution progresses. In w_I the clusters consist of even numbers of sign changes and the function is predominantly positive, while in w_{II} they are odd numbered and the function changes sign between clusters. The sign change clusters become narrow in just the same way that the spikes in P do, and indeed the two types of feature coincide. The narrowing, together with the inaccuracies in the data at the spikes, makes determining the precise behaviour of sign changes within a cluster difficult. However, careful examination suggests that while the width of a cluster tends to zero, there is no cancellation between the sign changes.

Given the large numbers of terms in the expressions for the curvature invariants, relating their behaviour to features of P , Q and λ is not a simple matter. However, by comparing the magnitudes of individual terms we have found that at late times we can approximate the curvature invariants with simplified expressions

$$w_I \approx \frac{1}{32} e^{3\tau - \lambda} (A^2 + 3)(A^2 - 1)^2, \quad (4.4a)$$

$$w_{II} \approx -\frac{1}{16} e^{2\tau + P - \lambda} D A (A + 3)(A - 1)(A + 1)^2. \quad (4.4b)$$

These approximations fail when the values they predict are small: other terms in the curvature invariants clearly cannot be neglected then. The sign changes in w_I are all clustered around the positive spikes in P , and this makes sense in terms of the approximation since $-1 < A < +1$ is found everywhere except at these spikes. (The terms neglected in (4.4a) turn out to be negative at the spikes.) The behaviour of w_{II} is similar, except for the influence of D in equation (4.4b). At each positive spike in P there is a zero of D together with an odd number of sign changes in w_{II} . Zeros of D at points where no spikes develop produce isolated sign changes in w_{II} . However, although a pair of zeros appears in D where a double spike forms in Q , no unusual behaviour occurs in w_{II} there. It seems that zeros in A counteract the effect of the zeros in D sufficiently so that terms neglected in equation (4.4b) become significant and prevent w_{II} from changing sign.

(We note that the sign change clusters in w_I and w_{II} evolve at different rates, and this leads to some discrepancies between figure 4 and the behaviour described in the paragraph above. By

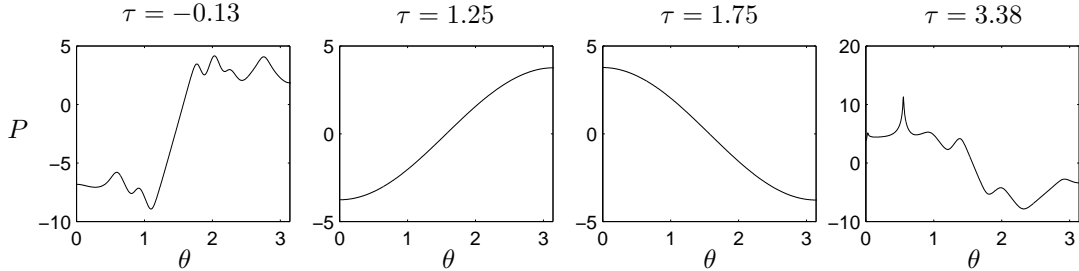


Figure 5: Development of small-scale structure in P for evolution both forwards and backwards in time. Initial data (2.9) with $v_0 = 15$ is used at starting time $\tau = 1.5$. The left two plots are produced by evolving backwards from this initial state, the right two plots by evolving forwards.

time $\tau = 6\pi$ some of the clusters are already too narrow to be resolved and inaccuracies at the double spikes are large enough to cause the invariants to behave erratically there.)

It follows that the formation of positive spikes in P is more than a coordinate effect induced by the form of the Gowdy metric, and is connected with unusual behaviour of the spacetime curvature. On the other hand our results suggest that this may not be the case for the double spikes that form in Q : while both P and Q can be related to the proper lengths of the trajectories of the metric's T^2 isometry group, the spiky behaviour of Q does not seem to have a physical effect beyond this.

If we extrapolate the observed behaviour of the curvature invariants forward in time to the singularity at $\tau = \infty$ we see that they become infinite—except possibly at isolated values of θ corresponding to the positive spikes in P . This is in agreement with the curvature behaviour at the singularity conjectured by Moncrief [13]. (The same reference shows that no curvature singularities can develop before $\tau = \infty$, and our results do not suggest otherwise.)

The main features of the behaviour reported above are also found in simulations using initial data other than equation (2.9) or a starting time other than $\tau = 0$, and the implication is that the behaviour is reasonably generic. It is interesting to ask, though, what behaviour the spacetime must have prior to the starting time in order that it arrives at the initial state we have chosen—that is, what happens if we start with initial data (2.9) but reverse the direction of time? We find that, in general, the variables P and Q have a simple wave motion away from the singularity, as equations (2.4) suggest, but that for a starting time closer to the singularity (e.g., $\tau > 4$) or a large value for the parameter v_0 in (2.9) small-scale spatial structure again starts to form. (This is illustrated in figure 5.) However, in this case the small-scale structure does not grow indefinitely and eventually the wave motion takes over. Even when small-scale structure is developing, the curvature invariants are found to be rapidly approaching zero, and the spacetime ‘flattens’ as it expands.

5 The AVTD and VTDB Hypotheses

Although the VTDB hypothesis of Eardley *et al* [5] is difficult to formulate in a covariant manner, it is easy to interpret it for this problem. In our evolution equations (2.3) and (2.4) (combined in (2.7)) every spatial derivative is multiplied by a factor $\exp(-\tau)$. Since the singularity is given by $\tau \rightarrow +\infty$, it might seem reasonable to ignore these terms when studying the singularity. The resulting system of ordinary differential equations can be solved analytically and one finds

$$P(\tau, \theta) \sim a_0(\theta)\tau, \quad Q(\tau, \theta) \sim q_0(\theta) \quad \text{as } \tau \rightarrow \infty. \quad (5.1)$$

The numerical evidence in favour of this asymptotic behaviour is compelling: $B \equiv Q_\tau$ and $A_\tau \equiv P_{\tau\tau}$ tend to zero as τ increases. Thus we can confirm Berger and Moncrief's assertion in [3] that the Gowdy T^3 cosmologies exhibit AVTD behaviour.

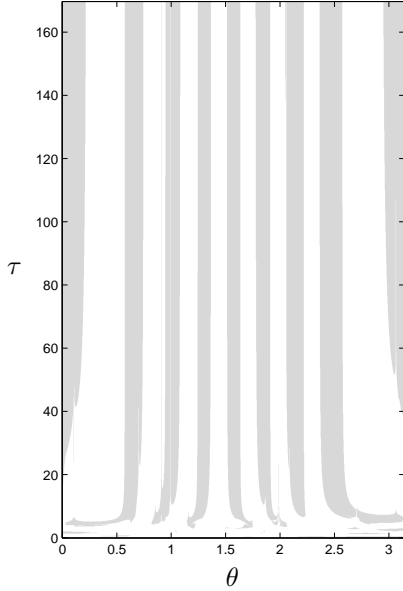


Figure 6: The VTDB region for $\tau \leq 54\pi$. Spatial derivatives are considered negligible in the shaded regions, which correspond to the intersection of the light grey regions from both halves of figure 3.

However, there is no evidence that the VTDB hypothesis used to derive (5.1) is valid! The light-grey regions in figure 3 show where spatial derivative terms are unimportant in the two wave equations, and examination of their intersection reveals that for $\tau \leq 6\pi$ there are intervals of θ in which VTDB occurs, but that they do not cover the whole range of θ . Figure 6 shows these VTDB regions for an extended time range, $\tau \leq 54\pi$. Clearly the behaviour is not universal.

In a recent preprint, Kichenassamy and Rendall [11] have examined analytically the behaviour of the Gowdy T^3 cosmologies near the singularity. Their results seem to suggest that the asymptotic behaviour (5.1) is universal, and is therefore not contingent on the VTDB hypothesis.

6 Conclusions

We have two groups of conclusions, one for cosmology and one for numerical relativity. We have investigated structure formation and behaviour near the singularity in the Gowdy T^3 cosmologies.

- Our calculations are consistent with the earlier ones of Berger and Moncrief [3], but show more fine-scale structure.
- This fine-scale structure is not a coordinate effect since it also occurs in the curvature invariants.
- As claimed earlier there is considerable numerical evidence that the AVTD conjecture is valid for the Gowdy T^3 cosmologies, but there is no evidence to support the hypothesis of VTDB. Although spatial derivative terms matter, this does not seem to affect the asymptotic evolution near the singularity.
- The Gowdy T^3 cosmologies have the unexpected property that smooth initial data acquires structure when it is evolved both backwards and forwards in time.

We have not investigated in detail the symplectic integrator used by Berger and Moncrief, but for this problem it would seem to perform no better than standard finite-difference methods. A simple Lax-Wendroff code using 8000 grid points without AMR will produce results that differ from those shown in figure 1 only at the points where spiky features develop. However, the AMR code is faster and allows details smaller than the coarse grid spacing to be investigated. Summarizing the advantages AMR brings for this problem:

- Results (on the coarsest grid) with the required level of overall accuracy are produced in minimal time.
- Small spatial features are resolved without requiring a high density of grid points everywhere on the domain.
- The total number of grid points changes with time and allows quick evolution of the ‘frozen’ spatial structures found at late times.
- No prediction as to the amount of fine-scale structure that will develop is needed beforehand.

There is another, subtle feature of AMR. We have been asked frequently why Lax-Wendroff with AMR gives results which are indistinguishable from the highly sophisticated CLAWPACK codes. At first sight the Lax-Wendroff scheme would appear to be inappropriate: it contains artificial viscosity which would smear out the spatial structure we observe. However the viscosity coefficient is $O((\Delta\theta)^2)$ where $\Delta\theta$ is the spatial grid spacing, and when spatial structure is encountered the AMR code evolves it with a very small $\Delta\theta$ so that consequently there is very little dissipation.

We thank Neil Cornish for useful discussions, and Beverly Berger, David Garfinkle and Vincent Moncrief for encouragement. Simon Hern was supported by an EPSRC studentship.

References

- [1] V.A. Belinskii, I.M. Khalatnikov & E.M. Lifschitz, *Advances in Physics*, **19**, 525 (1970); *ibid.* **31**, 639 (1982).
- [2] B.K. Berger, in *Proceedings of the 14th International Conference on General Relativity and Gravitation*, edited by M. Francaviglia, G. Longhi, L. Lusanna & E. Sorace, World Scientific (1997).
- [3] B.K. Berger & V. Moncrief, *Phys. Rev.*, **D48**, 4676 (1993).
- [4] M.J. Berger & J. Oliger, *J. Comp. Phys.*, **53**, 484 (1984).
- [5] D. Eardley, E. Liang & R. Sachs, *J. Math. Phys.*, **13**, 99 (1972).
- [6] R.H. Gowdy, *Phys. Rev. Lett.*, **27**, 826 (1971); *ibid.* **27**, E1102 (1971); *Ann. Phys. (NY)*, **83**, 203, (1974).
- [7] B. Grubišić & V. Moncrief, *Phys. Rev.*, **D47**, 2371 (1993).
- [8] R. Hamadé & J.M. Stewart, *Class. Quantum Grav.*, **13**, 497 (1996).
- [9] S.W. Hawking & G.F.R. Ellis, *The Large Scale Structure of Space-time*, Cambridge (1973).
- [10] J. Isenberg & V. Moncrief, *Ann. Phys. (NY)*, **199**, 84 (1990).
- [11] S. Kichenassamy & A.D. Rendall, *Class. Quantum Grav.*, **15**, 1339 (1998).
- [12] R.J. LeVeque, *J. Comp. Phys.*, **131**, 327 (1997).
- [13] V. Moncrief, *Ann. Phys. (NY)*, **132**, 87 (1981).
- [14] M.H.P.M. van Putten, *Phys. Rev.*, **D55**, 4705 (1997).
- [15] D.S. Salopek & J.M. Stewart, *Phys. Rev.*, **D51**, 517 (1995).